

REGULARIZING INR WITH DIFFUSION PRIOR FOR SELF-SUPERVISED 3D RECONSTRUCTION OF NEUTRON COMPUTED TOMOGRAPHY DATA

Maliha Hossain, Haley Duba-Sullivan, Amirkoushyar Ziabari

Oak Ridge National Laboratory, 1 Bethel Valley Road, Oak Ridge, TN, USA 37830

ABSTRACT

Recently, generative diffusion priors have made huge strides as inverse problem solvers, including the ability to be adapted for inference on out-of-distribution data. Concurrently, implicit neural representations (INRs) have emerged as fast and lightweight inverse imaging solvers that are amenable to hybrid approaches that combine learned priors with traditional inverse problem formulations. In this paper, we present a diffusive computed tomography (CT) inversion framework for regularizing INRs called Diffusive INR (DINR), designed to enable high-quality reconstruction from sparse-view neutron CT. Pretrained purely on synthetic data, DINR is evaluated on simulated and experimentally obtained observations of concrete microstructures, where traditional reconstruction methods suffer substantial degradation when the number of views is reduced. Our approach delivers superior performance, reduces reconstruction artifacts, and achieves gains in PSNR and SSIM, enabling accurate micro-structural characterization even under extreme data limitations compared to state-of-the-art sparse-view reconstruction techniques.

Index Terms— Neutron CT, Inverse Problems, Diffusion, Implicit Neural Representation

1. INTRODUCTION

Neutron Computed Tomography (CT) is an important imaging modality due to its unique ability to characterize volumes by hydrogen distribution [1]. This capability is critical in a number of settings, including manufacturing hydrogen fuel cells [2] and lithium-ion batteries [3], studying water transport in plants and soil [4, 5], and safety monitoring of concrete components for radiation shielding and structural integrity [6, 7]. Conventional CT reconstruction, generally using projection measurements with a few thousand views, is performed using analytical methods such as Filtered Back Projection (FBP). Many CT applications necessitate sparse view sampling for fast acquisition, such as real-time surgical guidance, security screening, etc. Neutron CT, in particular,

due to its low beam flux, requires much longer exposure times to achieve measurements with acceptable signal-to-noise ratio [8]. However, FBP typically cannot handle view sparsity below Nyquist without generating severe artifacts [9], motivating the development of model-based iterative reconstruction (MBIR) that includes a prior model term in a cost function formulation. MBIR requires hand-constructed priors such as Total Variation (TV) and other Markov random fields of higher orders like qGGMRF [10, 11]. However, diffusion-based inverse problem solvers are able to model more complex image properties and are at the forefront of powerful generative priors for solving ill-posed inverse problems [12, 13].

Sparse-view CT is an ill-posed inverse problem that occurs when the scanner collects fewer projection views than required by the Nyquist sampling theorem [9]. There have been several notable advances in unsupervised deep learning-based approaches for solving inverse imaging problems.

Implicit neural representations (INRs) [14] have emerged as a powerful tool in the field of 3D imaging by learning to use neural networks to represent a volume with a continuous function. While this in turn allows them to capture a reconstructed volume with a memory-efficient and resolution-independent representation, standard implicit neural representations exhibit a strong spectral bias toward low-frequency components, which can lead to poor reconstruction of high-frequency structure and unstable behavior when supervision is sparse or ill-conditioned [15]. However, their ability to easily integrate learned priors and CT forward models makes them a powerful tool to be exploited in conjunction with other advanced prior modeling techniques [16, 17].

Steerable Conditional Diffusion (SCD) [12] is an effective approach for leveraging measurement data to guide a pre-trained diffusion model towards a target distribution at test time. SCD alternates between updating the diffusion model weights and producing an estimate for posterior mean. In [13], the authors propose DD3IP, a 3D Deep Diffusion Image Prior, which is a generalization of SCD that can coherently reconstruct across orthogonal spatial dimensions in a 3D volume of out-of-distribution (OOD) parallel beam CT data using a UNet denoising diffusion model. One key contribution of DD3IP is the conclusion that posterior sampling in SCD can be performed agnostically of the choice of diffusion inverse problem solver (DIS), resulting in a modular framework where we can plug in state of the art CT measurement inversion models. In this work, we build on that conclusion as follows:

1. We formulate a regularized INR DIS within a DD3IP framework and demonstrate its ability to generate high-

Corresponding author's email address: ziabariak@ornl.gov. This manuscript has been authored by UT-Battelle, LLC, under contract DE-AC05-00OR22725 with the US Department of Energy (DOE). The US government retains and the publisher, by accepting the article for publication, acknowledges that the US government retains a nonexclusive, paid-up, irrevocable, worldwide license to publish or reproduce the published form of this manuscript, or allow others to do so, for US government purposes. DOE will provide public access to these results of federally sponsored research in accordance with the DOE Public Access Plan (<https://www.energy.gov/doe-public-access-plan>).

quality sparse-view parallel-beam neutron CT reconstructions. Our INR incorporates the denoised diffusion output into a proximal formulation of the INR loss function.

2. Our software implementation improves on [13]’s by adopting a distance driven parallel beam projector from Tomosipo, a pythonic wrapper for the ASTRA-toolbox to enforce data consistency, and for better modularity. Our code and data will be made available online.
3. We present a comparison against MBIR with a qG-GMRF prior, which is a more realistic model than the more commonly presented TV prior. DINR can perform on par with qGGMRF in sparse-view reconstruction and even outperform it in the ultra-sparse regime.

2. BACKGROUND

2.1. Implicit Neural Representations (INRs)

INRs model images or volumes as continuous functions parameterized by a neural network, typically a multilayer perceptron that maps spatial coordinates to signal values, e.g., attenuation coefficients [18, 14]. A widely used INR architecture is the sinusoidal representation network (SIREN) [14], which employs periodic sinusoidal activation functions in each layer of an MLP to better represent high-frequency content. The coordinate-based formulation of INRs enables resolution-independent reconstruction, differentiable sampling, and compact encoding of entire volumes within a small set of network weights. INRs can be optimized directly against measured CT projections and flexibly integrated with physics-based forward models and learned priors, making them attractive for model-based or plug-and-play reconstruction. Recent works have demonstrated INR-based approaches for sparse-view and limited-angle CT, leveraging implicit functions to jointly learn geometry and attenuation while regularizing through learned priors or deep image prior [16, 17]. Extensions to this framework have incorporated additional input channels, such as FDK reconstructions, to provide an initial estimate that accelerates convergence and improves reconstruction quality [19]. However, INR-based reconstructions can be slow to optimize and may lack strong image priors unless combined with architectural regularization (e.g., dropout) or learned denoisers [20, 21].

2.2. 3D Deep Diffusion Image Prior (DD3IP)

A standard denoising diffusion probabilistic model (DDPM) [22] consists of a forward process, where Gaussian noise is gradually added to a sample, and a reverse process, where a neural network is trained to denoise each step. Denoising diffusion implicit models (DDIMs) [23] were introduced as an efficient and deterministic variant of standard diffusion models. SCD can "steer" or guide a pretrained inverse imaging diffusion prior to adapt to an OOD inference sample at test-time. Instead of using the fixed DDIM reverse process, SCD applies gradient-based updates to guide the sample toward OOD data. [13] showed that SCD is a special case of Deep Image Prior and formulated a coherent multi-slice reconstruction framework for parallel beam CT that alternates

between adapting the diffusion model weights for OOD inference data and sampling from the posterior using DDIM. They further showed that the resulting DD3IP framework is agnostic of the strategy to estimate the posterior mean in the DDIM step as long as it is informed by the weight-adapted diffusion model.

3. METHOD

Let $y = Ax + n$, where x is a 3D tensor of attenuation coefficient values mapped over a volumetric lattice S , y is its corresponding projection, A is a parallel beam CT projection matrix, and n is additive noise approximating the actual noise in the measurement. The analytical solution of this problem $x = A^*y$ can be found using FBP.

SCD can be presented in a deep image prior framework as

$$\text{for } t = T \dots 1 : \theta_{t-1} \leftarrow \arg \min_{\theta_t} \text{MSE}(y, AD_{\theta_t}(x_t|y)) \quad (1)$$

$$x_{t-1} \leftarrow DDIM_{\theta_{t-1}}(D_{\theta_{t-1}}(x_t|y), \eta) \quad (2)$$

where $t \in [0, T]$ is the diffusion time-step variable, θ_t is the diffusion model weights at time t , D_{θ_t} is the denoising diffusion model, and x_t is the estimate at time t . Additionally, $\eta \in [0, 1]$ is a random variable that controls stochasticity and MSE is the mean squared error loss. DDIM sampling is given by

$$DDIM_{\theta}(\hat{x}_t, \eta) := \sqrt{\alpha_{t-1}}\hat{x}_t + \sqrt{1 - \alpha_{t-1}}(\eta\epsilon + (1 - \eta)\epsilon^{\theta}), \quad (3)$$

where $\alpha_{1:T} \in (0, 1]^T$ is a decreasing sequence that parameterizes the reverse diffusion process [23], ϵ is spherically interpolated Gaussian noise [13], and ϵ^{θ} is the noise removed by D_{θ} .

The INR model F_{ϕ} with associated weights ϕ is trained to map coordinates in the cubic lattice S to attenuation coefficient values. Our INR is formulated to also accept the FBP estimate, A^*y , as an input to further inform reconstruction as in [16]. Since the INR is regularized by the diffusion model, we additionally include the current diffusion model estimate $\hat{x}_t = D_{\theta_t}(x_t|y)$ in the loss to be minimized. Altogether, we define a proximal loss for updating the INR weights:

$$\mathcal{L}_{\phi}(S, y, \hat{x}_{0|t}, \rho) = \text{MSE}(AF_{\phi}(S, A^*y), y) + \rho \text{MSE}(\hat{x}_t, F_{\phi}(S, A^*y)), \quad (4)$$

where ρ is a user-defined parameter controlling the influence of the diffusion model estimate. When we initialize the INR weights, we use $\rho = 0$, which gives the standard MSE loss. Since \hat{x} is not needed in this case, we use the notation $\mathcal{L}_{\phi_{t-1}}(S, y, -, \rho = 0)$. The resulting DDIM sampling including the INR is given by $DDIM_{\theta_{t-1}}(F_{\phi_{t-1}}(S, A^*y), \eta)$ where $\phi_{t-1} = \arg \min_{\phi} \mathcal{L}_{\phi}(S, y, \hat{x}_t, \rho)$.

We replicate the initialization strategy from [13] where the diffusion model weights are pretrained on synthetic ellipsoid data and x_T is initialized at the start of the reverse diffusion process as

$$x_T \leftarrow \sqrt{\alpha_T}A^*y + \sqrt{1 - \alpha_T}\epsilon * w, \quad (5)$$

where A^*y represents the low frequency component of the solution corrupted with ϵ . We additionally introduce a tunable scaling parameter $\omega > 0$ to the noise injection which controls the regularization of the DD3IP methods by scaling the values of A^*y relative to the noise variance of ϵ . Our reconstruction algorithm is presented in Algorithm 1.

Algorithm 1 DINR Algorithm

```

1:  $S \leftarrow$  3D coordinate grid
2:  $A \leftarrow$  sparse-view parallel beam projector
3:  $y \leftarrow$  sparse-view CT projection
4:  $\phi_T \leftarrow \arg \min_{\phi} \{ \mathcal{L}_{\phi}(S, y, -, \rho = 0) \}$ 
5:  $\theta_T \leftarrow$  pretrained diffusion weights
6:  $x_T \leftarrow \sqrt{\alpha_T} A^*y + \sqrt{1 - \alpha_T} \epsilon * w$ 
7: for  $t = T$  to 1 timesteps: do
8:    $\theta_{t-1} \leftarrow \arg \min_{\theta} \{ \text{MSE}(AD_{\theta}(x_t|y), y) \}$ 
9:    $\hat{x}_t \leftarrow D_{\theta_{t-1}}(x_t|y)$ 
10:   $\phi_{t-1} \leftarrow \arg \min_{\phi} \{ \mathcal{L}_{\phi}(S, y, \hat{x}_t, \rho) \}$ 
11:  if  $t == 1$  then
12:     $x_{t-1} \leftarrow F_{\phi_{t-1}}(S, A^*y)$ 
13:  else
14:     $x_{t-1} \leftarrow DDIM_{\theta_{t-1}}(F_{\phi_{t-1}}(S, A^*y), \eta)$ 
15:  end if
16: end for
17: Return  $x_0$ 

```

4. RESULTS

In this section, we present data reconstruction results from both simulated and real observations of concrete cylinder cross-sections in an neutron CT scanner system and compare the results of our proposed method, DINR, against traditional FBP reconstructions as well as two state-of-the-art (SOTA) methods, DD3IP [13] and Siren [14] (which we refer to as INR). Additionally, we present reconstructions of the real dataset made using MBIR with a finely tuned qGGMRF prior.

The simulated phantom is a $2 \times 256 \times 256$ volume whose first slice is shown in Figure 1(a). The phantom is forward projected with the tomosipo parallel beam projector at different view sparsities. The reconstruction from the sinograms using the aforementioned methods are presented in Figure 2 and corresponding performance metrics measured in PSNR and SSIM are presented in Table 1. For the DD3IP reconstruction, we use the default parameters for learning rates, epochs, etc, provided for the UNet demo in the github associated with [13], except the number of CG steps for the DIS is increased to 200. For both DD3IP and DINR, ω is parameter swept to maximize PSNR. For DINR, ρ was chosen so that the ratio of the proximal term to the data fidelity term in \mathcal{L}_{ϕ} equaled $1e - 5$.

The experimental sinogram is obtained from a neutron CT scanner with 1091 view angles spanning 360° , 2048 slices and 1048 detectors per view. A full-view sample is reconstructed using MBIR with a qGGMRF prior using pyMBIR software [24] (Figure 1(b)) and used as reference for computing metrics in Table 2. To suppress noise and artifacts in the raw projection data, a 7×7 median filter was applied, and a regularization parameter sweep was performed to ob-

Table 1: PSNR (dB)/SSIM comparison for different views (synthetic data). Best results are shown in bold

Views	FBP	INR	DD3IP	DINR
4	19.31/0.08	14.76/0.18	26.17/ 0.25 ($\omega = 0.02$)	26.27 /0.24 ($\omega = 0.2$)
8	21.67/0.18	28.15/0.35	28.37/0.34 ($\omega = 0.2$)	28.56 / 0.38 ($\omega = 0.02$)
16	25.27/0.30	30.34/0.54	31.21/0.61 ($\omega = 0.02$)	31.3 / 0.63 ($\omega = 0.02$)
32	29.62/0.43	32.85/0.66	32.91/0.74 ($\omega = 0.002$)	33.43 / 0.76 ($\omega = 0.02$)

Table 2: PSNR (dB)/SSIM comparison for different number of views (real data). While MBIR and DD3IP have comparable PSNR/SSIM, DINR produces higher visual quality reconstructions for ultra-space scans (Figure 3), highlight the needs for better quantitative metrics in future work.

Views	FBP	MBIR	INR	DD3IP	DINR
5	19.9/0.1	21.02/0.04	20.18/0.03	20.89/ 0.06	21.27 /0.05
9	22.9/0.33	26 / 0.38	24.08/0.27	25.41/0.34	25.22/0.35
17	25.91/0.55	28.1 /0.58	27.3/0.54	28.04/ 0.62	27.56 / 0.62
33	30.11/0.73	31/0.77	29.7/0.71	31.19/ 0.79	31.37 /0.77

tain the MBIR reconstruction with the highest local signal-to-noise ratio (SNR) between the foreground and background regions of the reconstructed volume. The real sinogram (detector data) was then trimmed to 1024 detectors per view and downsampled to 256, and the central two slices were reconstructed at various view sparsities. Specifically, the original 545 view angles between 0° and 180° were sub-sampled by factors of 16, 32, 64, and 128, resulting in scans with 5, 9, 17, and 33 views, as summarized in Table 2. Reconstructions for each experiment are shown in Figure 3. For DD3IP and DINR, we set $\omega = 0.002$. Additionally, for DINR, ρ was chosen such that the ratio of the proximal term to the data-fidelity term in \mathcal{L} was 1×10^{-6} , which yielded the optimal PSNR scores. For MBIR reconstruction of the sparse-view data, a full logarithmic sweep of the regularization parameter from 10^{-4} to 10^6 was performed to identify the optimal value, i.e. the one yielding the best reconstruction quality compared to the ground truth, at each sparsity level. This configuration is then used for comparison against the deep learning-based methods. While such exhaustive parameter tuning is computationally intractable for large-scale datasets, it ensures a fair and unbiased evaluation by benchmarking our method against the best achievable MBIR performance.

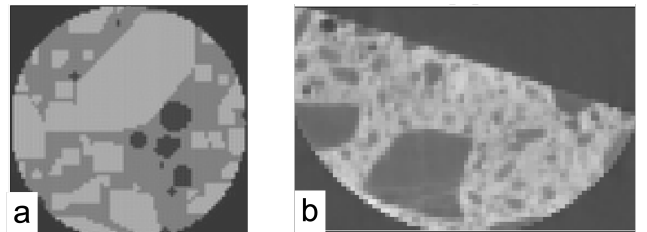


Fig. 1: Reference reconstruction for comparison with images in Figures 2 and 3, as well to calculate metrics in Tables 1 and 2.

One of the key challenges in evaluating reconstruction

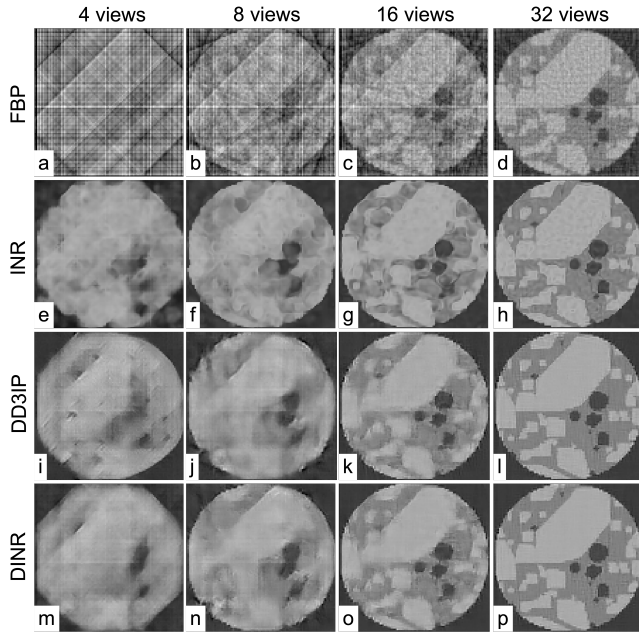


Fig. 2: Reconstruction of synthetic data. The columns and rows in panels a-p are annotated to distinguish different experiments. DINR overall preserves the boundary and texture (pores/microstructure) very well, even for a 4-view ultra-sparse scan.

quality for scientific imaging data lies in defining an appropriate region of interest (ROI) where an algorithm performs best. In the literature, ROI-based metrics are often computed using manually defined masks; however, this approach assumes prior knowledge of where to mask and introduces user bias, which is particularly problematic for microstructure data with irregular geometries. To minimize this bias, we adopt a consistent, data-driven approach. We first identify the largest region within the field of view that contains both the object and background without visible artifacts in the ground-truth reconstruction, an area of 64×96 pixels. From this region, smaller subregions of 64×64 , 48×48 , 32×32 , 16×16 , and 8×8 pixels are cropped systematically, ensuring automatic and unbiased ROI selection. Within each subregion, PSNR is computed for all reconstruction methods.

As shown in Figure 4, for reconstructions with 5, 9, 17, and 33 views, the DINR method demonstrates superior performance within regions dominated by microstructural features rather than background, particularly for ROIs smaller than 48×48 pixels and most notably below 32×32 pixels. This indicates that DINR achieves higher fidelity within the microstructure, while inclusion of background regions reduces its relative advantage and allows other techniques to attain similar quantitative metrics. This trend is also qualitatively evident in the 5/9-view MBIR reconstruction results, where the overall MBIR reconstruction quality in Figure 3(e)-(f) appears worse than DD3IP and DINR, yet the MBIR method yields higher PSNR in ROIs that include a larger portion of the background.

This analysis is conceptually analogous to the *SNR growth-curve* or *task-based detectability* methods used in CT image-quality evaluation, where SNR is analyzed as a function of ROI size to assess spatial resolution and local

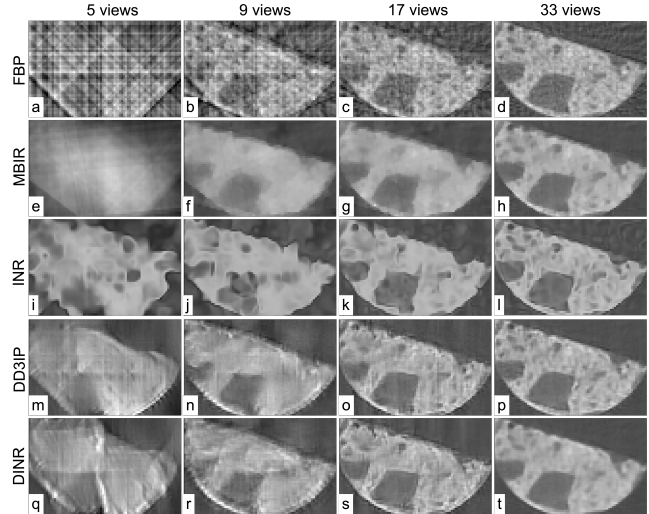


Fig. 3: Reconstruction of real data. The columns and rows in panels a-t are annotated to distinguish different experiments. DINR overall preserves the boundary and texture (pores/microstructure) very well, even for a 5-view ultra-sparse scan.

contrast fidelity. Future work will focus on developing more discriminative metrics based on segmentation of particles and boundaries within the microstructure to further refine quantitative evaluation.

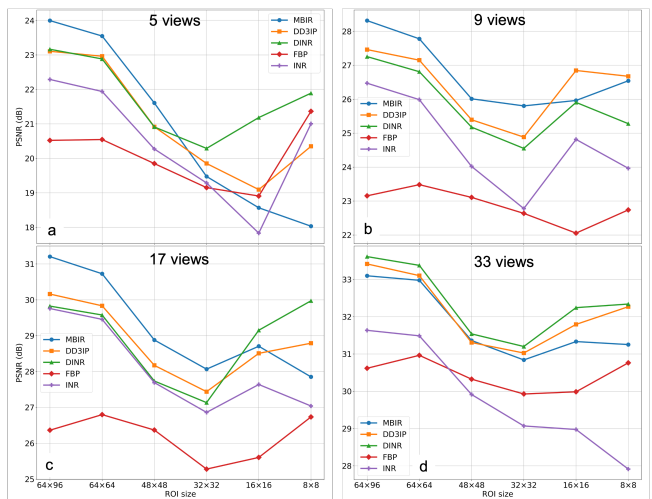


Fig. 4: PSNR calculated systematically for varying ROI to mask the impact of the background and compare performance in reducing artifacts within microstructure region for a) 5 views, b) 9 views, c) 17 views, and d) 33 views.

5. CONCLUSION

We proposed DINR for sparse-view CT reconstruction and demonstrated its capabilities over a state-of-the-art diffusion inverse solver and INR. In particular, we demonstrated results for synthetic and real neutron CT of microstructure data, and observed that even with a small number of views (min. 5 in our test data), our proposed DINR produces higher quality reconstructions than SOTA approaches. However, the efficacy of our method for handling view sparsity can be ex-

tended to other CT beam sources such as X-ray, or electron CT. In future work, we intend to conduct a comprehensive ablation study to evaluate the contribution of the FBP input to both INR and DINR reconstructions. Furthermore, we anticipate that a more exhaustive parameter search will establish that DINR can outperform MBIR across a broader range of imaging conditions. Finally, we plan to extend our software framework to support multi-GPU implementations, enabling the reconstruction of larger volumetric datasets and facilitating the application of DINR to more advanced CT acquisition geometries, including cone-beam and helical CT and extend our work to other CT applications that require sparse view sampling.

6. REFERENCES

- [1] Nikolay Kardjilov, Ingo Manke, André Hilger, Markus Strobl, and John Banhart, “Neutron imaging in materials science,” *Materials Today*, vol. 14, no. 6, pp. 248–256, 2011.
- [2] Ralf F Ziesche, Jennifer Hack, and et al., “High-speed 4d neutron computed tomography for quantifying water dynamics in polymer electrolyte fuel cells,” *Nature Communications*, vol. 13, no. 1, pp. 1616, 2022.
- [3] Ralf F Ziesche, Tobias Arlt, and et al., “4d imaging of lithium-batteries using correlative neutron and x-ray tomography with a virtual unrolling technique,” *Nature communications*, vol. 11, no. 1, pp. 777, 2020.
- [4] Christian Tötze, Nikolay Kardjilov, Ingo Manke, and Sascha E Oswald, “Capturing 3d water flow in rooted soil by ultra-fast neutron tomography,” *Scientific reports*, vol. 7, no. 1, pp. 6192, 2017.
- [5] Paiman Shafabakhsh, Benoît Cordonnier, and et al., “4d neutron imaging of solute transport and fluid flow in sandstone before and after mineral precipitation,” *Water Resources Research*, vol. 60, no. 3, pp. e2023WR036293, 2024.
- [6] Great S Anunike, Mohamad Tarabin, and Ousmane A Hisseine, “Ultra-high-performance concrete for nuclear applications: A review of raw materials and mix design approaches,” *Construction and Building Materials*, vol. 438, pp. 136938, 2024.
- [7] Mingfei Yan, Yasuo Wakabayashi, and et al., “Reconstruction on fast neutron ct for concrete structure inspection with a pixel-type detector by applying linear scanning method,” in *EPJ Web of Conferences*. EDP Sciences, 2020, vol. 231, p. 05008.
- [8] Shengxiang Wang, Jianfang Li, and et al., “Fstu-net: A sparse-view ct reconstruction framework for enhanced imaging efficiency and quality in neutron tomography,” *Nuclear Instruments and Methods in Physics Research Section A: Accelerators, Spectrometers, Detectors and Associated Equipment*, p. 170524, 2025.
- [9] Wenrui Li, Gregory T Buzzard, and Charles A Bouman, “Sparse-view ct reconstruction using recurrent stacked back projection,” in *2021 55th Asilomar Conference on Signals, Systems, and Computers*. IEEE, 2021, pp. 862–866.
- [10] Charles Bouman and Ken Sauer, “A generalized gaussian image model for edge-preserving map estimation,” *IEEE Transactions on image processing*, vol. 2, no. 3, pp. 296–310, 1993.
- [11] Singanallur Venkatakrishnan et al., “Algorithm-driven advances for scientific CT instruments: From model-based to deep learning-based approaches,” *IEEE Signal Processing Magazine*, vol. 39, no. 1, pp. 32–43, 2021.
- [12] Riccardo Barbano, Alexander Denker, and et al., “Steerable conditional diffusion for out-of-distribution adaptation in imaging inverse problems,” *CoRR*, 2023.
- [13] Hyungjin Chung and Jong Chul Ye, “Deep diffusion image prior for efficient ood adaptation in 3d inverse problems,” in *European Conference on Computer Vision*. Springer, 2024, pp. 432–455.
- [14] Vincent Sitzmann, Julien Martel, Alexander Bergman, David Lindell, and Gordon Wetzstein, “Implicit neural representations with periodic activation functions,” *Advances in neural information processing systems*, vol. 33, pp. 7462–7473, 2020.
- [15] Matthew Tancik, Pratul Srinivasan, and et al., “Fourier features let networks learn high frequency functions in low dimensional domains,” *Advances in neural information processing systems*, vol. 33, pp. 7537–7547, 2020.
- [16] Ruyi Zha, Yanhao Zhang, and Hongdong Li, “Naf: neural attenuation fields for sparse-view cbct reconstruction,” in *International Conference on Medical Image Computing and Computer-Assisted Intervention*. Springer, 2022, pp. 442–452.
- [17] Jiayang Shi, Junyi Zhu, Daniel M Pelt, K Joost Batenburg, and Matthew B Blaszka2022nafhko, “Implicit neural representations for robust joint sparse-view ct reconstruction,” *arXiv preprint arXiv:2405.02509*, 2024.
- [18] Jeong Joon Park, Peter Florence, and et al., “Deepsdf: Learning continuous signed distance functions for shape representation,” in *Proceedings of the IEEE/CVF conference on computer vision and pattern recognition*, 2019, pp. 165–174.
- [19] Li Zhou, Changsheng Fang, and et al., “ ρ -nerf: leveraging attenuation priors in neural radiance field for 3d computed tomography reconstruction,” in *2025 IEEE International Conference on Image Processing (ICIP)*. IEEE, 2025, pp. 1636–1641.
- [20] Nasim Rahaman, Aristide Baratin, and et al., “On the spectral bias of neural networks,” in *International conference on machine learning*. PMLR, 2019, pp. 5301–5310.

- [21] Sameera Ramasinghe, Lachlan Ewen MacDonald, Moshir Farazi, Hemanth Saratchandran, and Simon Lucey, “How much does initialization affect generalization?” in *International Conference on Machine Learning*. PMLR, 2023, pp. 28637–28655.
- [22] Jonathan Ho, Ajay Jain, and Pieter Abbeel, “Denoising diffusion probabilistic models,” *Advances in neural information processing systems*, vol. 33, pp. 6840–6851, 2020.
- [23] Jiaming Song, Chenlin Meng, and Stefano Ermon, “Denoising diffusion implicit models,” *arXiv preprint arXiv:2010.02502*, 2020.
- [24] Singanallur V. Venkatakrishnan, “pyMBIR,” <https://github.com/svvenkatakrishnan/pyMBIR>, Accessed: 2021–2022.